

Central Path Art

Thor Catteau^{*a1*}, Benjamin Glancy^{*a2*}, Allen Holder^{*a3**}, Angela Milkowski^{*a4*}, Alexa Renner^{*a5*}, Connor Tasik^{*a6*}, and Rebecca Testa^{*a7*}

^{*a*} Department of Mathematics, Rose-Hulman Institute of Technology,
Terre Haute, IN, USA

¹ catteae@rose-hulman.edu, ² glancybc@rose-hulman.edu

³ holder@rose-hulman.edu, ⁴ milkowaj@rose-hulman.edu

⁵ renneram@rose-hulman.edu, ⁶ tasikca@rose-hulman.edu

⁷ testarl@rose-hulman.edu

*Corresponding author

October 3, 2025

Abstract

The central path revolutionized the study of optimization in the 1980s and 1990s due to its favorable convergence properties, and as such, it has been investigated analytically, algorithmically, and computationally. Past pursuits have primarily focused on linking iterative approximation algorithms to the central path in the design of efficient algorithms to solve large, and sometimes novel, optimization problems. This algorithmic intent has meant that the central path has rarely been celebrated as an aesthetic entity in low dimensions, with the only meager exceptions being illustrative examples in textbooks. We undertake this low dimensional investigation and illustrate the artistic use of the central path to create aesthetic tilings and flower-like constructs in two and three dimensions, an endeavor that combines mathematical rigor and artistic sensibilities. The result is a fanciful and enticing collection of patterns that, beyond computer generated images, supports math-aesthetic designs for novelties and museum-quality pieces of art.

Keywords: Optimization, Central Path, Mathematical Art

1 Historical Basis and Motivation

The concepts of an analytic center and an interior point algorithm began with Frisch and Huard at the inception of the modern age of optimization and operations research [6, 12, 13], see also the original work of Dikin [3] and Fiacco and McCormick [4]. These pioneering articles motivated the idea of iterating

through points interior to the feasible region toward an optimal solution, which differed from the prevailing vertex approach of the simplex method. However, the simplex algorithm left open the question of whether or not the class of linear programming problems was solvable in polynomial time [18]. Leonid Khachiyan famously answered this question in 1979 by presenting a polynomial time algorithm for linear programs [17], but Khachiyan’s algorithm proved impractical and the simplex method continued to prevail until Narendra Karmarkar introduced a more successful polynomial time algorithm in 1984 [15, 16]. Although not obvious at the time of their publications, the algorithms of both Khachiyan and Karmarkar were interior-point methods related to the original works of Huard, Dikin, and Fiacco and McCormick, a connection that was noticed soon thereafter in [7]. The practical and mathematical success of Karmarkar’s algorithm marked the advent of interior-point methods, and it led to thousands upon thousands of publications that have revolutionized the field of optimization [5, 27, 28]. An overriding conclusion from this literature is that efficient and efficacious solution procedures to a wide class of salient problems rely on the favorable convergence properties of the central path, and hence, the central path is one of the most important mathematical entities of the twentieth century.

The central path is a parametrization of the positive real half-line in a convex set, and each element of the path is an analytic center. The pertinence of the central path to effective algorithm design has prompted numerous mathematical studies to understand its analytic, geometric, and topological properties. Sonnevend undertook many of the original studies [23, 24], see also [14], but the mathematical pursuits continued for decades as briefly illustrated by [1, 2, 9, 11, 19, 20, 26]. We refer readers to see [25] for a succinct historical review of interior point methods.

Our motivation to create art with the central path stems from its mathematical and computational properties, which again, have revolutionized the field of optimization. Many have generated paths in low dimensions to limn the behavior of interior-point methods, and in doing so, they have certainly found it easy, if not alluring, to be captivated by an esoteric and quizzical elegance. We leverage this elegance to create aesthetic images in two and three dimensions, and we use these images to create artistic wall hangings, works of stained glass, backpack tags, beverage coasters, holiday ornaments, and three-dimensional sculptures. A continued pursuit is to assemble three-dimensional sculptures into an optimization garden full of (random) interior bouquets that dance and sparkle.

We straightforwardly introduce the central path and its convergence analysis in Sections 2 and 3 so that it is reasonably accessible to undergraduates, although many will require modest educational additions. For instance, few undergraduates have dedicated coursework in optimization and/or convex analysis, and standard courses in real analysis often forgo the Implicit Function Theorem. We employ such results and expect readers to undertake brief studies as needed. We also encourage the use of the *Mathematical Programming Glossary* to clarify definitions [22].

We present two- and three-dimensional works of art in Sections 4.1 and 4.2. Our projects separate into two categories, one based on tilings of k -gons and another based on floral facsimiles, e.g. daisies, thistles, tulips, roses, and trumpet flowers. The majority of our work to date stems from central paths in two-dimensions, but we also demonstrate the use of Platonic solids. Some of our designs have motivated new mathematical relationships — so the quest to create art has lead to a bit of new mathematics. We conclude in Section 5 with a succinct review and a discussion of our future goals.

2 The Analytic Central Path

The specific model from which we proceed is important because the central path depends on the algebraic description of an optimization problem and not directly on its geometry, a fact first recognized by Sonnevend [23] and then analyzed in [1]. We assume that

$$G : \mathbb{R}^n \rightarrow \mathbb{R}^m : x \mapsto \begin{pmatrix} g_1(x) \\ g_2(x) \\ \vdots \\ g_m(x) \end{pmatrix}$$

is twice smooth, that $\nabla G(x)$ has full column rank, and that each component function is convex. The assumed convexity of each $g_i(x)$ ensures that

$$\{x : G(x) \leq 0\}$$

is convex. We further assume that this set is compact and that its strict interior is nonempty, i.e. $\{x | G(x) < 0\} \neq \emptyset$. The assumption of compactness is atypical but apt for our purposes. Our mathematical model is

$$\max \left\{ c^T x + \mu \sum_{i=1}^m \ln(s_i) : G(x) + s = 0, s \geq 0 \right\}, \quad (1)$$

with $c \in \mathbb{R}^n$ defining a linear term in the objective function and μ being a positive parameter. The objective function maps into the extended reals, $\bar{\mathbb{R}} = \mathbb{R} \cup \{-\infty, \infty\}$, with the objective value being $-\infty$ if some $s_i = 0$.

Our first result shows that (1) is well-posed.

Theorem 1. *The optimization problem in (1) is well-posed for $\mu > 0$ under the stated assumptions of G .*

Proof. We have feasibility by assumption, and the objective function is continuous over the strict interior of the feasible region. Moreover, if $(x^k, s^k) \rightarrow (\hat{x}, \hat{s})$ is a convergent sequence of feasible elements, then

$$\limsup_{k \rightarrow \infty} \left(c^T x^k + \mu \sum_{i=1}^m \ln(s_i^k) \right) \leq \left(c^T \hat{x} + \mu \sum_{i=1}^m \ln(\hat{s}_i) \right).$$

This inequality follows if $\hat{s} > 0$ because the objective function is then continuous at (\hat{x}, \hat{s}) , and consequently, the limit supremum is finite and we satisfy the inequality as an equality. If $\hat{s}_i = 0$ for some i , then any subsequence of (x^k, s^k) , say (x^{k_j}, s^{k_j}) , satisfies $s_i^{k_j} \rightarrow 0$ as $j \rightarrow \infty$, and hence, the left-hand side is $-\infty$, which matches the right-hand in this case. We conclude that the objective is upper semicontinuous, which establishes the result because upper semicontinuous functions attain their maximums over compact sets. \blacksquare

We assume for notational convenience that capitalized vectors represent diagonal matrices whose main diagonals are the elements of the vector, so if x is an n -vector, then X is an $n \times n$ diagonal matrix such that $X_{ii} = x_i$. We further use $A > 0$ ($A < 0$) and $A \succeq 0$ ($A \preceq 0$) to indicate respectively that A is either positive (negative) definite or positive (negative) semidefinite. Letting $f(x, s)$ be the objective function in (1), we have with these notational conventions that the Hessian of $f(x, s)$ at a strictly feasible point (x, s) satisfies

$$\nabla^2 f(x, s) = \begin{bmatrix} 0 & 0 \\ 0 & -S^{-2} \end{bmatrix} \leq 0.$$

So the objective function is concave over the strict interior of the feasible set. If any component of s^1 or s^2 is zero for the feasible elements (x^1, s^1) and (x^2, s^2) , then we also have

$$f((1-\theta)x^1 + \theta x^2, (1-\theta)s^1 + \theta s^2) \geq (1-\theta)f(x^1, s^1) + \theta f(x^2, s^2) = -\infty.$$

So the objective function is concave, and subsequently, the optimization problem in (1) is convex.

The Lagrangian of (1) is

$$\mathcal{L}(x, s, y, \sigma) = c^T x + \mu \sum_{i=1}^m \ln(s_i) - y^T (G(x) + s) - \sigma^T s,$$

and the convexity of the problem means that the first-order Lagrange conditions are both necessary and sufficient for optimality. So (x, s) is optimal if and only if there are m -vectors y and σ so that,

$$\nabla_{x,s} \mathcal{L}(x, s, y, \sigma) = \begin{pmatrix} c - \nabla G(x)^T y \\ \mu S^{-1} e - y - \sigma \end{pmatrix} = \begin{pmatrix} 0 \\ 0 \end{pmatrix},$$

$$G(x) + s = 0, \quad \sigma^T s = 0, \quad s \geq 0, \quad \text{and } \sigma \geq 0,$$

with e being the vector of ones and length being decided by the context of its use. Note that s has positive components in an optimal solution, and hence, we know that $s > 0$, $\sigma \geq 0$, and $\sigma^T s = 0$, from which we gain that $\sigma = 0$. Also note that $\mu S^{-1} e - y = 0$ ensures that $y > 0$ because $\mu > 0$. So if we re-express $\mu S^{-1} e - y = 0$ as $Sy - \mu e = 0$, then the necessary and sufficient conditions reduce

to,

$$\left. \begin{array}{lcl} \nabla G(x)^T y - c & = & 0, \quad y > 0, \\ G(x) + s & = & 0, \quad s > 0, \text{ and} \\ Sy - \mu e & = & 0. \end{array} \right\} \quad (2)$$

We define F to be

$$F : \mathbb{R}^{2m+n+1} \rightarrow \mathbb{R}^{2m+n} : (x, s, y, \mu) \mapsto \begin{pmatrix} \nabla G(x)^T y - c \\ G(x) + s \\ Sy - \mu e \end{pmatrix},$$

so that the necessary and sufficient conditions for $\mu > 0$ are succinctly,

$$F(x, s, y, \mu) = 0 \quad \text{and} \quad (s, y) > 0. \quad (3)$$

We now have

$$\nabla_{x,s,y} F(x, s, y, \mu) = \begin{bmatrix} \sum_{i=1}^m y_i \nabla^2 g_i(x) & 0 & \nabla G(x)^T \\ \nabla G(x) & I & 0 \\ 0 & Y & S \end{bmatrix},$$

and we argue that this matrix is invertible, from which we gain that x and s are analytic functions of μ from the Implicit Function Theorem.

Lemma 1. *Assume that Q and D are $n \times n$ matrices and that B is an $m \times n$ matrix. Further assume that $Q \succeq 0$, $D > 0$, and that B has full column rank. Then*

$$\begin{bmatrix} Q & B^T \\ DB & -I \end{bmatrix}$$

is nonsingular.

Proof. Observe that

$$\begin{bmatrix} Q & B^T \\ DB & -I \end{bmatrix} \begin{pmatrix} w \\ u \end{pmatrix} = \begin{pmatrix} 0 \\ 0 \end{pmatrix}$$

reduces to

$$(Q + B^T DB) w = 0.$$

The properties of Q , B , and D ensure that $Q + B^T DB > 0$, from which we conclude that w , and subsequently u , are both zero. \blacksquare

Theorem 2. *There is a unique solution to (1) for each $\mu > 0$, say $x(\mu)$, $s(\mu)$ and $y(\mu)$, all of which are twice-smooth functions of μ .*

Proof. We first observe that

$$\begin{bmatrix} \sum_{i=1}^m y_i \nabla^2 g_i(x) & 0 & \nabla G(x)^T \\ \nabla G(x) & I & 0 \\ 0 & Y & S \end{bmatrix} \begin{pmatrix} u \\ v \\ w \end{pmatrix} = \begin{pmatrix} 0 \\ 0 \\ 0 \end{pmatrix}$$

gives $v = -\nabla G(x)u$ and $Yv + Sw = 0$. So we can replace the bottom two equalities with

$$-Y \nabla G(x) u + Sw = 0, \text{ which is the same as } S^{-1}Y \nabla G(x) u - w = 0.$$

So the system reduces to

$$\begin{bmatrix} \sum_{i=1}^m y_i \nabla^2 g_i(x) & \nabla G(x)^T \\ S^{-1}Y \nabla G(x) & -I \end{bmatrix} \begin{pmatrix} u \\ w \end{pmatrix} = \begin{pmatrix} 0 \\ 0 \end{pmatrix}. \quad (4)$$

We know that

$$\sum_{i=1}^m y_i \nabla^2 g_i(x) \succeq 0$$

because each $g_i(x)$ is twice smooth and convex, and hence, each Hessian satisfies $\nabla^2 g_i(x) \succeq 0$. Lemma 1 now ensures that the matrix in (4) is nonsingular with

$$Q = \sum_{i=1}^m y_i \nabla^2 g_i(x) \succeq 0, \quad B = \nabla G(x), \quad \text{and} \quad D = S^{-1}Y > 0.$$

So u and w are zero, and subsequently, so is v . We conclude that $\nabla_{x,s} F(x, s, \mu)$ is nonsingular, and the result follows from the Implicit Function Theorem. \blacksquare

We comment that the functions $x(\mu)$, $s(\mu)$, and $y(\mu)$ inherit the analytic properties of $G(x)$ from the Implicit Function Theorem. So these functions are, for instance, analytic in the common situation that the component functions of $G(x)$ are analytic. We note further that x , s , and y also depend on the data that defines $G(x)$ and c . So if $G(x)$ is the affine transformation $G(x) = Ax - b$, then x , s , and y depend on μ as well as the triple (A, b, c) , a fact that leads to additional analyses, see [10, 23].

Our artistic goals prompt us to define the central path as

$$\mathbf{P}(G(x), c) = \{x(\mu) : \mu > 0\},$$

which, somewhat oddly, lacks an explicit dependence on $s(\mu)$ and/or $y(\mu)$. The elements of s are slack variables in the language of optimization, and we have included them to simplify our calculations. The elements of y are Lagrange,

or dual, variables in optimization, and they give us a way to define optimality conditions algebraically. Explicitly including s or y as part of the central path places us in dimensions beyond visual appeal, and for this reason, our definition projects $\{(x(\mu), s(\mu), y(\mu)) : \mu > 0\}$ onto its x -components. We create art by controlling $G(x)$ and c , with each choice rendering a ‘brushstroke’ in two or three dimensions. We then assemble these brushstrokes into aesthetic ensembles.

3 Convergence Analysis

We most commonly use the affine map $G(x) = Ax - b$ even though some of our floral pieces more naturally align with $G(x)$ being a quadratic form. However, in these cases we show that an affine map still suffices, and hence, the majority, and indeed all but one, of our models uses an affine map computationally. The only computational quadratic case is one in which we can explicitly state the central path. Otherwise the affine map combines with our assumption of a bounded feasible region to give central paths in polytopes, an outcome that supports a meaningful and insightful convergence analysis. We specifically show that $x(\mu)$ converges as $\mu \uparrow \infty$ and as $\mu \downarrow 0$, and moreover, that these limits solve optimization problems that distinguish them as analytic centers. Our presentation is not new and is found, for instance, in [21].

We now assume that $G(x) = Ax - b$, from which we have that the necessary and sufficient conditions in (2) become

$$Ax + s = b, \quad A^T y = c, \quad Sy = \mu e, \quad y > 0, \quad s > 0. \quad (5)$$

We first establish that solutions to this system are bounded if $s^T y$ is bounded.

Theorem 3. *The set*

$$\mathcal{B} = \{(x, y, s) : Ax + s = b, A^T y = c, y > 0, s > 0, s^T y \leq M\}$$

is bounded for any $M > 0$.

Proof. Select $M > 0$ and $(\hat{x}, \hat{y}, \hat{s}) \in \mathcal{B}$. We then have for any other $(x, y, s) \in \mathcal{B}$ that $\hat{s} - s \in \text{col}(A)$ and $\hat{y} - y \in \text{null}(A^T)$, and hence,

$$0 = (\hat{s} - s)^T (\hat{y} - y) = \hat{s}^T \hat{y} - s^T \hat{y} - \hat{s}^T y + s^T y.$$

So for any index i , we have

$$\hat{s}_i y_i \leq \hat{s}^T y + s^T \hat{y} = \hat{s}^T \hat{y} + s^T y \leq \hat{s}^T \hat{y} + M,$$

and subsequently,

$$0 \leq y_i \leq \frac{\hat{s}^T \hat{y} + M}{\hat{s}_i}.$$

An analogous argument shows that for any index i ,

$$0 \leq s_i \leq \frac{\hat{s}^T \hat{y} + M}{\hat{y}_i},$$

which completes the proof because we also know that x is bounded by assumption. \square

We have the following corollary from the fact that $Sy = \mu e$ implies $s^T y = m\mu$.

Corollary 1. *If $\mu^k \downarrow 0$, then the solutions to (5) are bounded.*

We now show that $x(\mu)$ converges as $\mu \downarrow 0$ and as $\mu \uparrow \infty$, with the former limit solving the linear program,

$$\max\{c^T x : Ax + s = b, s \geq 0\}.$$

The fact that we can solve a linear optimization problem by following the central path as $\mu \downarrow 0$ is the historical reason for the path's importance, and in particular, following the central path to a solution leads to polynomial time algorithms. Our artistic pursuits do not rely on this historical importance, but the convergence properties help us understand the 'starting' and 'ending' points of the paths used to create images. Both limits are analytic centers.

Our arguments rely on the concept of a support set, which for vector v is

$$\sigma(v) = \{i : v_i \neq 0\}.$$

So the support set of v is an index set containing the locations at which v is non-zero. We extend this notation in two ways. First, the complement of $\sigma(v)$ is $\neg\sigma(v) = \{1, 2, \dots, n\} \setminus \sigma(v)$ under the assumption that v is of length n . Second, $v_{\sigma(v)}$ is the subvector of v containing only the non-zero elements of v (with order preserved), and similarly, $v_{\neg\sigma(v)}$ is a vector of zeros.

Theorem 4. *The following limits exist,*

$$\lim_{\mu \downarrow 0} (x(\mu), s(\mu)) = (x^*, s^*) \quad \text{and} \quad \lim_{\mu \uparrow \infty} (x(\mu), s(\mu)) = (x^c, s^c),$$

and the first of these solves $\max\{c^T x : Ax + s = b, s \geq 0\}$. We further have that (x^*, s^*) is the unique solution to

$$\max \left\{ \sum_{i \in \sigma(s^*)} \ln(s_i) : Ax + s = b, s_{\sigma(s^*)} > 0, s_{\neg\sigma(s^*)} = 0, c^T x = c^T x^* \right\}, \quad (6)$$

and that (x^c, s^c) is the unique solution to

$$\max \left\{ \sum_{i=1}^m \ln(s_i) : Ax + s = b, s > 0 \right\}. \quad (7)$$

Proof. Assume $\mu^k \downarrow 0$ and set $(x^k, y^k, s^k) = (x(\mu^k), y(\mu^k), s(\mu^k))$. This sequence is bounded by Corollary 1, and hence, it has a cluster point, say (x^*, y^*, s^*) . Without loss of generality, we assume $(x^k, y^k, s^k) \rightarrow (x^*, y^*, s^*)$ as $k \rightarrow \infty$. We have from the fact that (x^k, y^k, s^k) satisfies (5) that

$$Ax^* + s^* = b, A^T y^* = c, s^* \geq 0, y^* \geq 0, \text{ and } (s^*)^T x^* = 0.$$

These are the necessary and sufficient conditions showing that (x^*, s^*) and y^* respectively solve

$$\max\{c^T x : Ax + s = b, s \geq 0\} \quad \text{and} \quad \min\{b^T y : A^T y = c, y \geq 0\}. \quad (8)$$

Notice that $s^k - s^* \in \text{col}(A)$ and $y^k - y^* \in \text{null}(A^T)$, and hence, from the fact that $s_i^k y_i^k = \mu^k$ for any index i , we have

$$\begin{aligned} 0 &= (s^k - s^*)^T (y^k - y^*) \\ &= (s^k)^T y^k - (s^*)^T y^k - (s^k)^T y^* + (s^*)^T y^* \\ &= m\mu^k - (s^*)^T y^k - (s^k)^T y^*. \end{aligned}$$

We subsequently have

$$m = \sum_{i \in \sigma(s^*)} \frac{s_i^*}{s_i^k} + \sum_{i \in \sigma(y^*)} \frac{y_i^*}{y_i^k},$$

from which we gain that $\sigma(s^*)$ and $\sigma(y^*)$ partition $\{1, 2, \dots, m\}$. So (x^*, y^*, s^*) is a strictly complementary solution to the primal-dual pair in (8), from which we know that if $(\bar{x}, \bar{y}, \bar{s})$ is an optimal solution to (8), then we are guaranteed to have $\sigma(\bar{s}) \subseteq \sigma(s^*)$ and $\sigma(\bar{y}) \subseteq \sigma(y^*)$.

To see that (x^*, s^*) uniquely solves (6), let $(\bar{x}, \bar{y}, \bar{s})$ be an arbitrary optimal solution to (8). Then an analogous argument to that above shows that

$$m = \sum_{i \in \sigma(s^*)} \frac{\bar{s}_i}{s_i^k} + \sum_{i \in \sigma(y^*)} \frac{\bar{y}_i}{y_i^k},$$

and the arithmetic-geometric mean inequality gives

$$\prod_{i \in \sigma(s^*)} \left(\frac{\bar{s}_i}{s_i^k} \right) \prod_{i \in \sigma(y^*)} \left(\frac{\bar{y}_i}{y_i^k} \right) \leq \frac{1}{m} \left(\sum_{i \in \sigma(s^*)} \frac{\bar{s}_i}{s_i^k} + \sum_{i \in \sigma(y^*)} \frac{\bar{y}_i}{y_i^k} \right) = 1.$$

One choice for \bar{y} is y^* , and in this case we have

$$\prod_{i \in \sigma(s^*)} \bar{s}_i \leq \prod_{i \in \sigma(s^*)} s_i^k.$$

So as $\mu^k \downarrow 0$, we find that (x^*, s^*) solves

$$\max \left\{ \prod_{i \in \sigma(s^*)} s_i : Ax + s = b, s_{\sigma(s^*)} > 0, s_{\neg\sigma(s^*)} = 0, c^T x = c^T x^* \right\},$$

which means that it also solves

$$\max \left\{ \sum_{i \in \sigma(s^*)} \ln(s_i) : Ax + s = b, s_{\sigma(s^*)} > 0, s_{\neg\sigma(s^*)} = 0, c^T x = c^T x^* \right\}.$$

The assumed full column rank of A ensures that x and s are in a one-to-one relationship, and specifically, $x = (A^T A)^{-1} A^T (b - s)$ is the same as $Ax + s = b$. Moreover, the constraint $s_{\neg\sigma(s^*)} = 0$ means that these variables are fixed, and hence, x is in a one-to-one relationship with $s_{\sigma(s^*)}$. This means that $s_{\sigma(s^*)}^*$ solves

$$\max \left\{ \sum_{i \in \sigma(s^*)} \ln(s_i) : A(A^T A)^{-1} A^T (b - s) = b - s, \right. \\ \left. s_{\sigma(s^*)} > 0, s_{\neg\sigma(s^*)} = 0, c^T (A^T A)^{-1} A^T (b - s) = c^T x^* \right\}.$$

The Hessian of the objective function is $-S_{\sigma(s^*)}^{-2} < 0$. So the objective function is strictly concave and the solution is unique. We consequently have that (x^*, s^*) solves (6).

Now assume $\mu^k \uparrow \infty$ and again set $(x^k, y^k, s^k) = (x(\mu^k), y(\mu^k), s(\mu^k))$. The sequence (x^k, s^k) is in a compact feasible region by assumption, and it therefore has a cluster point, say (x^c, s^c) . We assume without loss of generality that $(x^k, s^k) \rightarrow (x^c, s^c)$ is a convergent subsequence as $k \rightarrow \infty$. Let $(\bar{x}, \bar{y}, \bar{s})$ be feasible to the linear programs in (8). Then $s^k - \bar{s} \in \text{col}(A)$ and $y^k - \bar{y} \in \text{null}(A^T)$, and similar to the orthogonal arguments above, we have

$$\frac{\bar{s}^T \bar{y}}{\mu^k} + m = \sum_{i=1}^m \frac{\bar{y}_i}{y_i^k} + \sum_{i=1}^m \frac{\bar{s}_i}{s_i^k}.$$

Note that $s_i^k y_i^k = \mu^k$, so s^k being bounded forces $y_i^k \rightarrow \infty$ as $k \rightarrow \infty$. We now have that as $k \rightarrow \infty$,

$$m = \sum_{i=1}^m \frac{\bar{s}_i}{s_i^c},$$

and the arithmetic-geometric mean inequality gives,

$$\prod_{i=1}^m \bar{s}_i \leq \prod_{i=1}^m s_i^c.$$

So (x^c, s^c) solves,

$$\max \left\{ \prod_{i=1}^m s_i : Ax + s = b, s \geq 0 \right\},$$

and it thus also solves,

$$\max \left\{ \sum_{i=1}^m \ln(s_i) : Ax + s = b, s > 0 \right\}.$$

We express this problem uniquely in terms of s using the full column rank assumption of A , resulting in

$$\max \left\{ \sum_{i=1}^m \ln(s_i) : A(A^T A)^{-1} A^T (b - s) = b - s, s > 0 \right\}.$$

The Hessian of the objective function is $-S^{-2} < 0$, from which we know that (x^c, s^c) is the unique solution to (7). So all convergent subsequences of $(x(\mu^k), s(\mu^k))$ converge to (x^c, s^c) , and hence, $(x(\mu^k), s(\mu^k))$ converges to (x^c, s^c) . \blacksquare

Theorem 4 guarantees that the closure of the central path is

$$\overline{\mathbf{P}(G(x), c)} = \mathbf{P}(G(x), c) \cup \{x^c, x^*\},$$

and we assume computationally that paths start at x^c , which will be the zero vector by design, and ends at x^* , i.e that μ starts at infinity and decreases to zero.

3.1 Computing Central Paths

Our description of the central path gives mathematical assurances, but we require a calculation method to generate images. The defining system with $G(x) = Ax - b$ is

$$F(x, s, y, \mu) = \begin{pmatrix} A^T y - c \\ Ax + s - b \\ Sy - \mu e \end{pmatrix} = \begin{pmatrix} 0 \\ 0 \\ 0 \end{pmatrix}, \quad \text{with } (y, s) > 0.$$

We use Newton's method to estimate $x(\mu)$, $s(\mu)$, and $y(\mu)$ from any x , s , and y by iteratively solving

$$\left. \begin{aligned} \nabla_{x,s,y} F(x, s, y, \mu) \begin{pmatrix} \Delta x \\ \Delta s \\ \Delta y \end{pmatrix} &= \begin{bmatrix} 0 & 0 & A^T \\ A & I & 0 \\ 0 & Y & S \end{bmatrix} \begin{pmatrix} \Delta x \\ \Delta s \\ \Delta y \end{pmatrix} \\ &= \begin{pmatrix} c - A^T y \\ b - Ax - s \\ \mu e - Sy \end{pmatrix} = -F(x, s, \mu) \end{aligned} \right\} \quad (9)$$

and updating x , s , and y so that

$$x \leftarrow x + \alpha \Delta x, \quad s \leftarrow s + \alpha \Delta s, \quad \text{and} \quad y \leftarrow y + \beta \Delta y.$$

The stepsizes α and β guarantee nonnegativity by setting them to

$$\alpha = \omega \min \{1, \min \{x_i / \Delta x_i : \Delta x_i < 0\}\}$$

$$\text{and} \quad \beta = \omega \min \{1, \min \{y_i / \Delta y_i : \Delta y_i < 0\}\},$$

with ω being a positive scalar that is less than one. The value of either inner minimum is ∞ if $\Delta x \geq 0$ or $\Delta y \geq 0$, respectively.

Calculating Δx , Δs , and Δy reduces to solving an $n \times n$ positive definite system to compute Δx , from which we then calculate Δs and Δy . We first notice the bottom two equations of the linear system in (9) give

$$A\Delta x + \Delta s = b - Ax - s \Rightarrow A^T S^{-1} Y (A\Delta x + \Delta s) = A^T S^{-1} Y (b - Ax - s)$$

and

$$Y\Delta s + S\Delta y = \mu e - Sy \Rightarrow A^T S^{-1} (Y\Delta s + S\Delta y) = A^T S^{-1} (\mu e - Sy).$$

Using $A^T \Delta y = c - A^T y$ from the first equation in (9) and combining these last two implications, we find that,

$$A^T S^{-1} Y A \Delta x = A^T S^{-1} Y (b - Ax - s) + c - \mu A^T S^{-1} e.$$

Our geometry permits a feasible starting point (x, s) , and in this case we know that $Ax + s = b$ with $s > 0$. In this situation we have $A\Delta x + \Delta s = 0$ from the second equation in (9), and hence, $(x + \alpha \Delta x, s + \alpha \Delta s)$ remains feasible after the update because

$$A(x + \alpha \Delta x) + (s + \alpha \Delta s) = Ax + s = b.$$

Moreover, the equation defining Δx becomes

$$A^T S^{-1} Y A \Delta x = c - \mu A^T S^{-1} e. \quad (10)$$

We have $A^T S^{-1} Y A > 0$ because if v is a nonzero vector, then

$$v^T A^T S^{-1} Y A v = (\sqrt{S^{-1} Y} A v)^T (\sqrt{S^{-1} Y} A v) = \|\sqrt{S^{-1} Y} A v\|^2 > 0,$$

with $\sqrt{S^{-1} Y}$ being the diagonal matrix with diagonal elements $\sqrt{y_i/s_i}$. The positivity of $\|\sqrt{S^{-1} Y} A v\|$ follows from the fact that A has full column rank, and hence, neither Av nor $\sqrt{S^{-1} Y} A v$ are zero unless v is zero.

Solving (10) is efficient and numerically stable, see [29, 30], and once we have Δx , we set

$$\Delta s = -A \Delta x \quad \text{and} \quad \Delta y = \mu S^{-1} e - y - S^{-1} Y \Delta s.$$

The result is an efficient and numerically stable iterative process that efficiently converges to $x(\mu)$, $s(\mu)$, and $y(\mu)$. We cease iterations once

$$\max \{\|F(x, s, \mu)\|, \alpha \|\Delta x\|\} < \varepsilon, \quad (11)$$

with ε being a convergence tolerance.

Digitally rendering a central path necessitates that we compute a sequence, say μ^k , along with estimates for $x(\mu^k)$. We denote the estimates of $x(\mu^k)$, $s(\mu^k)$, and $y(\mu^k)$ as x^k , s^k , and y^k . The inequality in (11) ensures that

$$\|x^k - x(\mu^k)\| = \alpha \|\Delta x\| \leq \varepsilon.$$

So we guarantee accuracy to the central path at μ^k by decreasing ε , but this assurance leaves open the concern that we could lose accuracy as a graphics package interpolates estimates to create a curve. A common measure of how close a point (x, s, y) is to $(x(\mu^k), s(\mu^k), y(\mu^k))$ is

$$\|Sy - S(\mu^k)y(\mu^k)\| = \|Sy - \mu^k e\|, \quad (12)$$

see [26], and this measure promotes that we compute μ^k values so that

$$\max_{\theta} \left\{ \left\| \left((1-\theta)S^k + \theta S^{k+1} \right) \left((1-\theta)y^k + \theta y^{k+1} \right) - \mu^k e \right\| : 0 \leq \theta \leq 1 \right\} \leq \delta,$$

with δ being an allowed deviation from the central path. A straightforward calculation shows that the maximum is achieved at $\theta = 1/2$, and we initially devised a recursive bisection technique to ensure that

$$\frac{1}{4} \left\| \left(S^k + S^{k+1} \right) \left(y^k + y^{k+1} \right) - \mu^k e \right\| \leq \delta. \quad (13)$$

The process starts with μ^1 and μ^2 being respectively large and small enough so that $x^1 \approx x^c$ and $x^2 \approx x^*$. These approximations satisfy (11), and if they also satisfy (13), then we are done. We otherwise compute estimates

$$\begin{aligned} \hat{x} &\approx x((\mu^1 + \mu^2)/2), \\ \hat{s} &\approx s((\mu^1 + \mu^2)/2), \quad \text{and} \\ \hat{y} &\approx y((\mu^1 + \mu^2)/2), \end{aligned}$$

that satisfy (11) and renumber so that

$$\begin{aligned} (x^3, s^3, y^3, \mu^3) &\leftrightarrow (x^2, s^2, y^2, \mu^2) \quad \text{and} \\ (x^2, s^2, y^2, \mu^2) &\leftrightarrow (\hat{x}, \hat{s}, \hat{y}, (\mu^1 + \mu^2)/2). \end{aligned}$$

The process repeats on all $[\mu^k, \mu^{k+1}]$ intervals until each satisfies (13).

The μ^k list from the bisection technique with the standard measure in (12) proves problematic. The issue is that our central paths are approximated by the primal estimates, x^k , whereas the dual estimates, y^k , dominate the decisions of whether or not to bisect the intervals. The curvature of the dual central path does not align with the curvature of the primal, at least in our geometries, and the result is a list of μ^k values that over represent low curvature portions of the (primal) central path, see Figure 1.

We correct the overrepresentation of low curvature portions of the central path by estimating linearity with finite differences. If x^k , x^{k+1} , and x^{k+2} are consecutive estimates, then

$$T^k = \frac{x^{k+1} - x^k}{\|x^{k+1} - x^k\|} \quad \text{and} \quad T^{k+1} = \frac{x^{k+2} - x^{k+1}}{\|x^{k+2} - x^{k+1}\|}$$

approximate the unit tangent vectors of the central path at μ^k and μ^{k+1} . So estimates of the linearity of the central path over the intervals $[\mu^k, \mu^{k+1}]$ and

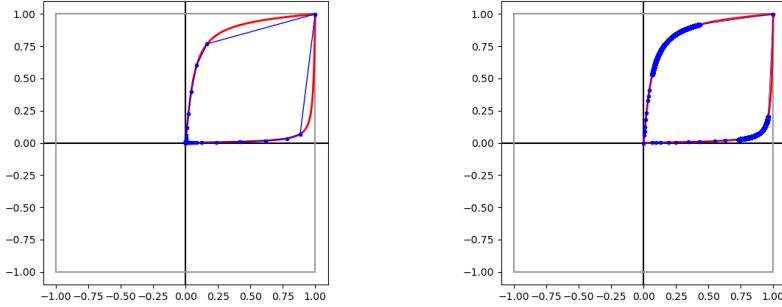


Figure 1: The figure on the left spaces μ with (13), and the figure on the right spaces μ by bounding (estimates) of curvature.

$[\mu^{k+1}, \mu^{k+2}]$ are respectively

$$\kappa^k = \frac{\|T^{k+1} - T^k\|}{\|x^{k+1} - x^k\|} \quad \text{and} \quad \kappa^{k+1} = \frac{\|T^{k+1} - T^k\|}{\|x^{k+2} - x^{k+1}\|}.$$

If $\kappa^k > \delta$, then we assume the central path is not sufficiently linear over $[\mu^k, \mu^{k+1}]$ and we bisect this interval by inserting the midpoint to our list of μ^k values. The same occurs if $\kappa^{k+1} > \delta$, but in this case we bisect $[\mu^{k+1}, \mu^{k+2}]$.

The bisection method based on our curvature estimates reduces the over representation of the central path on low curvature segments and increases accuracy on high curvature portions. Figure 1 compares the two techniques. The figure on the left sets $\delta = 0.08$ in (13), and the red central paths are approximated with 23 and 21 points. Notice how the majority of points accumulate near the center of the square and that the linear interpolation is less accurate as the path converges toward the upper right. The figure on the right instead bounds our curvature estimates by 0.5 and results in 8475 and 4208 points respectively for the top and bottom paths. Although the curvature tactic has more points than the bisection technique, we have the favorable outcome that the point estimates accumulate in regions of higher curvature.

3.2 Geometric Considerations

Affine transformations aid our geometric effort, and we establish that the central path of a transformed problem is the same as the transformation of the central path. This result is not unforeseen or unexpected, but it should not be assumed without proof because, as previously noted, the central path depends on the algebraic description of the problem and not on the geometry of the problem.

We illustrate this fact by observing that if

$$A = \begin{bmatrix} 1 & 0 \\ -1 & 0 \\ 0 & 1 \\ 0 & -1 \end{bmatrix} \quad \text{and} \quad \hat{A} = \begin{bmatrix} 1 & 0 \\ -1 & 0 \\ 0 & 1 \\ 0 & -1 \\ 1/2 & 1/2 \end{bmatrix},$$

then $Ax \leq e$ and $\hat{A}x \leq e$ are individually true if and only if $-1 \leq x_1 \leq 1$ and $-1 \leq x_2 \leq 1$. So

$$\{x : Ax \leq e\} = \{x : \hat{A}x \leq e\}.$$

However, setting $G(x) = Ax - b$ and $\hat{G}(x) = \hat{A}x - b$, we find that $\mathbf{P}(G(x), c) \neq \mathbf{P}(\hat{G}(x), c)$, as illustrated in Figure 2 with $c^T = (1, 2)$. The basic idea is that geometric intuition should draw caution because geometric perspective is coupled with, but disjoint from, algebraic exposition.

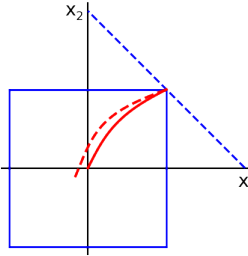


Figure 2: The solid central path ignores the dashed redundant constraint, whereas the dashed central path includes the redundant constraint.

Let $T(x) = Bx + d$ be an affine transformation with B being an invertible $n \times n$ matrix. Applying $T(x)$ to an element of the polytope $\{x : Ax \leq b\}$, we find that $T(x) = Bx + d = z$ if and only if $x = B^{-1}(z - d)$. This relationship gives the algebraic description of the image polytope as $\{z : AB^{-1}z \leq b + AB^{-1}d\}$. We now prove that central paths in $\{x : Ax \leq b\}$ correspond with central paths in the image polytope.

Theorem 5. *Let B be an invertible $n \times n$ matrix, and let $T(x) = Bx + d$. Set $G(x) = Ax - b$ and $\hat{G}(z) = AB^{-1}z - b - AB^{-1}d$. Then*

$$T(\mathbf{P}(G(x), c)) = \mathbf{P}(\hat{G}(z), (B^{-1})^T c).$$

Proof. We first note that $x(\mu) \in \mathbf{P}(G(x), c)$ if and only if there are unique $s(\mu)$ and $y(\mu)$ that satisfy

$$\begin{aligned} Ax + s &= b, \quad s \geq 0 \\ A^T y &= c, \quad y \geq 0 \\ Ys &= \mu e. \end{aligned}$$

Set $T(x(\mu)) = z(\mu)$ so that $x(\mu) = B^{-1}(z(\mu) - d)$. Then $z(\mu)$ satisfies

$$\begin{aligned} AB^{-1}z + s &= b + AB^{-1}d, \quad s \geq 0 \\ (B^{-1})^T A^T y &= (B^{-1})^T c, \quad y \geq 0 \\ Ys &= \mu e, \end{aligned}$$

which are the necessary and sufficient conditions for $z(\mu)$ to be the μ element of $\mathbf{P}(\hat{G}(z), (B^{-1})^T c)$. \square

We comment that the proof is stronger than the theorem statement because we have actually shown that the μ element of $\mathbf{P}(G(x), c)$ maps to the μ element of $\mathbf{P}(\hat{G}(z), (B^{-1})^T c)$.

Theorem 5 illustrates a mathematical and computational theme of our work, which is that we generate images with standard geometries and then translate them to create aesthetic images. Our most common two-dimensional polytope is the regular k -gon defined by $G^k(x) = Ax - e$, with the i -th row of the $k \times 2$ matrix A being

$$A_i^k = (\cos((i-1)2\pi/k), \sin((i-1)2\pi/k)).$$

We use the superscript k on both G and A to indicate this polygon. Consider the rotation matrix,

$$R(\theta) = \begin{bmatrix} \cos(\theta) & \sin(\theta) \\ -\sin(\theta) & \cos(\theta) \end{bmatrix},$$

and set $c^i(\theta) = A_i R(\theta)$, with A_i being the i -th row of A . Figure 3a displays $\mathbf{P}(G^3(x), c^i(\theta))$ for $i \in \{1, 2, 3\}$ and $\theta \in \{0.009, -0.009, 0.18, -0.18\}$, and Figure 3b displays $\mathbf{P}(G^6(x), c^i(\theta))$ for $i \in \{1, 2, \dots, 6\}$ and the same values of θ . Figure 3c displays a star created by translating the 3-gon paths around the 6-gon with the affine translations,

$$R\left(\frac{i\pi}{3}\right) \left(\begin{bmatrix} 1/3 & 0 \\ 0 & 1/3 \end{bmatrix} + \begin{pmatrix} -2 \\ 0 \end{pmatrix} \right),$$

with $i \in \{0, 1, 2, \dots, 5\}$. Theorem 5 ensures that the paths under translation are indeed paths within the translated polytopes. We comment that the objects in Figure 3 resemble k -gons by design, but they are not k -gons per se and are instead paths within k -gons.

Another use of Theorem 5 is the ability to create a font from central paths. We create characters from collections of ‘strokes,’ each of which equates with a translation of $\mathbf{P}(G^4(x), c)$, with c being decided to give an appropriate shape. The authors have taken to the moniker ‘InteriArt,’ and Figure 4 is an example of this term in characters rendered from 4-gon central paths. We also point out that we have replaced the traditional black square at the end of a proof with an emblem of paths in a 4-gon as a bit of artistic levity.

We have already seen in Figure 2 that different descriptions of the same geometry can lead to different central paths, and hence, it would be somewhat

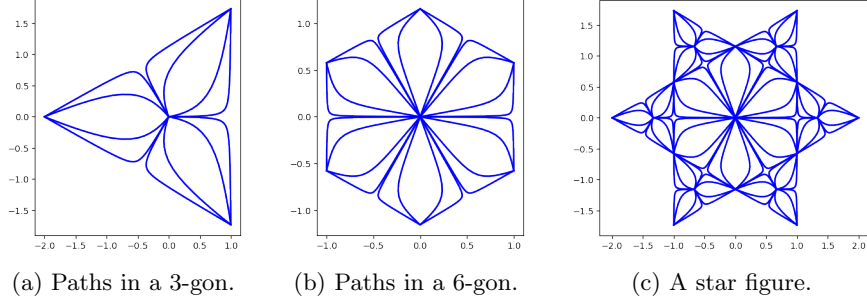


Figure 3: Translations of 3-gon paths form a star around a 6-gon.



Figure 4: A font created from central paths.

natural and analogous to assume that different geometries, which would necessarily have different algebraic descriptions, would also have different central paths. However, this is not a universal truth, and our final result shows that it is possible for central paths within different geometries and different algebraic descriptions to equate with each other. This result permits us to generate two-dimensional surfaces in three dimensions by generating a single path in a cube and then continually rotating it in three dimensions to form a surface.

Let

$$G^1(x) = \begin{pmatrix} x_1 - b_1 \\ x_2 - b_2 \\ x_3 - b_3 \\ -x_1 - b_1 \\ -x_2 - b_2 \\ -x_3 - b_3 \end{pmatrix} \text{ and } G^2(x) = \begin{pmatrix} x_1 - b_1 \\ -x_1 - b_1 \\ x_2^2 + x_3^2 - b_2^2 \end{pmatrix},$$

and consider the geometry in Figure 5, which assumes $b_1 = b_2 = 1$ for motivational purposes. The three-dimensional cube, $\{x : -1 \leq x_i \leq 1, i = 1, 2, 3\}$, is $\{x : G^1(x) \leq 0\}$, and this cube circumscribes the three-dimensional cylinder, $\{x : G^2(x) \leq 0\}$. Theorem 6 shows that central paths of the rotated cube equate with central paths in the cylinder.

Theorem 6. *Assume $c = (c_1, c_2, c_3)^T$ is such that $c_1 \neq 0$ and that at least one*

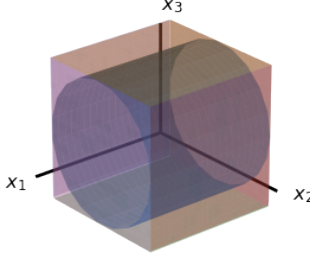


Figure 5: A right circular cylinder circumscribed by a cube.

of c_2 or c_3 is nonzero, and let R be the rotation matrix in the x_2 and x_3 plane,

$$R = \frac{1}{\sqrt{c_2^2 + c_3^2}} \begin{bmatrix} \sqrt{c_2^2 + c_3^2} & 0 & 0 \\ 0 & c_2 & c_3 \\ 0 & -c_3 & c_2 \end{bmatrix}.$$

Let $T(x) = Rx$ so that $T^{-1}(x) = R^{-1}x$. Then

$$T^{-1}(\mathbf{P}(G^1(x), T(c))) = \mathbf{P}(G^2(x), c).$$

Proof. The necessary and sufficient conditions in (3) for $\mathbf{P}(G^1, T(c))$, in block matrix form, are

$$\begin{bmatrix} I & -I \end{bmatrix} \begin{pmatrix} y_1 \\ y_2 \end{pmatrix} = T(c), \quad \begin{bmatrix} I \\ -I \end{bmatrix} x + \begin{pmatrix} s_1 \\ s_2 \end{pmatrix} = \begin{pmatrix} b \\ b \end{pmatrix}, \quad \text{and} \quad Sy = \mu e.$$

The middle equation asserts that $s_1 = b - x$ and $s_2 = b + x$, and substituting these into the third equality gives

$$y_1 = \mu(B - X)^{-1}e \quad \text{and} \quad y_2 = \mu(B + X)^{-1}e,$$

with both $B + X$ and $B - X$ being invertible because $0 < \mu < \infty$ ensures that $x(\mu)$ is strictly feasible, i.e. $-b < x < b$. The first equality now gives that

$$\mu((B - X)^{-1} - (B + X)^{-1})e = T(c)$$

defines $\mathbf{P}(G^1(x), T(c))$. Recognizing that

$$\begin{aligned} & (B - X)^{-1} - (B + X)^{-1} \\ &= ((B - X)(B + X))^{-1}(B - X)(B + X)((B - X)^{-1} - (B + X)^{-1}) \\ &= (B^2 - X^2)^{-1}((B + X) - (B - X)) \\ &= 2(B^2 - X^2)^{-1}X, \end{aligned}$$

we find that the elements of $\mathbf{P}(G^1(x), T(c))$ satisfy

$$2\mu(B^2 - X^2)^{-1}x = T(c),$$

which we re-express as

$$X^2T(c) + 2\mu x - B^2T(c) = 0. \quad (14)$$

We now have that the unique solution is

$$x_i(\mu) = \begin{cases} -\frac{\mu}{T(c)_i} + \frac{1}{|T(c)_i|}\sqrt{\mu^2 + T(c)_i^2 b_i^2}, & T(c)_i \neq 0 \\ 0, & T(c)_i = 0, \end{cases}$$

with $T(c)_i$ being the i -th component of $T(c)$. From the fact that

$$T(c) = \left(c_1, \sqrt{c_2^2 + c_3^2}, 0 \right)^T,$$

we have that the elements of $T^{-1}(\mathbf{P}(G^1(x), T(c)))$ are

$$R^{-1}x(\mu) = \begin{pmatrix} -\frac{\mu}{c_1} + \frac{1}{|c_1|}\sqrt{\mu^2 + c_1^2 b_1^2} \\ c_2 \left(\frac{-\mu + \sqrt{\mu^2 + (c_2^2 + c_3^2)b_2}}{c_2^2 + c_3^2} \right) \\ c_3 \left(\frac{-\mu + \sqrt{\mu^2 + (c_2^2 + c_3^2)b_2}}{c_2^2 + c_3^2} \right) \end{pmatrix}. \quad (15)$$

The necessary and sufficient conditions for $\mathbf{P}(G^2(x), c)$ are

$$\begin{aligned} \begin{bmatrix} 1 & -1 & 0 \\ 0 & 0 & 2x_2 \\ 0 & 0 & 2x_3 \end{bmatrix} \begin{pmatrix} y_1 \\ y_2 \\ y_3 \end{pmatrix} &= \begin{pmatrix} c_1 \\ c_2 \\ c_3 \end{pmatrix}, \\ \begin{pmatrix} x_1 \\ -x_1 \\ x_1^2 + x_2^2 \end{pmatrix} + \begin{pmatrix} s_1 \\ s_2 \\ s_3 \end{pmatrix} &= \begin{pmatrix} b_1 \\ b_1 \\ b_2^2 \end{pmatrix}, \text{ and } Ys = \mu e. \end{aligned}$$

Solving the second equality for s and substituting this expression into the third equality gives

$$y = \mu \begin{bmatrix} b_1 - x_1 & 0 & 0 \\ 0 & b_1 + x_1 & 0 \\ 0 & 0 & b_2^2 - x_2^2 - x_3^2 \end{bmatrix}^{-1} \begin{pmatrix} 1 \\ 1 \\ 1 \end{pmatrix},$$

with the inverse again being guaranteed because $0 < \mu < \infty$ ensures strict feasibility. Substituting this expression for y into the first condition gives

$$\mu \begin{bmatrix} 1 & -1 & 0 \\ 0 & 0 & 2x_2 \\ 0 & 0 & 2x_3 \end{bmatrix} \begin{pmatrix} 1/(b_1 - x_1) \\ 1/(b_1 + x_1) \\ 1/(b_2^2 - x_2^2 - x_3^2) \end{pmatrix} = \begin{pmatrix} c_1 \\ c_2 \\ c_3 \end{pmatrix}.$$

We rewrite these equations as

$$\begin{aligned} c_1 x_1^2 + 2\mu x_1 - b_1^2 c_1 &= 0, \\ c_2 (b_2 - x_2^2 - x_3^2) &= 2x_2 \mu, \text{ and} \\ c_3 (b_3 - x_2^2 - x_3^2) &= 2x_3 \mu. \end{aligned}$$

The first equation identifies x_1 exactly like (14), and hence, $x_1(\mu)$ is as stated in (15). The last two equations are coupled quadratics, and direct substitution of the second and third components of (15) satisfy these equations. \blacksquare

4 Artistic Outcomes

We now showcase several of our artistic projects, but we first note that the labor of creating quality art has been equal to, if not in excess of, our mathematical and computational efforts. Every art project has brought challenges and failures, and we have learned from each experience. Sometimes the hassle has been confronting technological limitations, sometimes it has been correcting standard image processing schemes, and sometimes it has been the slow, deliberate, and pedantic industry required to do most anything well. The projects that follow illustrate items that are the result of numerous previous attempts that were made before ‘getting things right.’ We catalog the effort associated with our largest piece to date in the attached supplement. Creating quality art is work, but it is also fulfilling and, in our case, it promotes how the mathematics of optimization is not only useful, but beautiful.

4.1 Two-Dimensional Art and Tilings

Central paths in two-dimensional k -gons combine to form appealing patterns useful in a variety of art projects, and we use these patterns to create a number of items. Most especially, two-dimensional paths lend themselves to laser cutting and etching and to 3D-printing. Our first 3D-print had random paths in a 4-gon, with each path being $\mathbf{P}(G^4(x), c)$ for a random c , see Figure 6a. Distributional qualities adjust appearance, and in this case we used two different distributions. If we visually divide the image into four “leaves” for descriptive purposes, then each leaf corresponds with one of the four vertices. Two paths define and bound each leaf, and we use a normal distribution to decide these paths. Let $\alpha \sim N(\eta, \sigma^2)$, and notice that each leaf is bracketed by paths defined by two rows of A^k . This is because $\mathbf{P}(G^4(x), A_i^4)$ is a line from the origin to the midpoint



(a) A 3D-print of paths in a 4-gon.

(b) A backpack tag.

Figure 6: Our original 3D-print of two-dimensional paths and a backpack tag from the same image.

of the facet defined by the supporting hyperplane $\{x : A_i^4 x = 1\}$. For instance, paths moving to the upper left have c vectors that are convex combinations of $A_2^4 = (0, 1)$ and $A_3^4 = (-1, 0)$. The paths in this object have $\eta = 0.0425$ and $\sigma = \eta/3$, and a pair of random samples, say α_1 and α_2 , define the two outer paths of each leaf. So the paths that define the leaf to the upper left have the form

$$c_1^T = (1 - \alpha)A_2^4 + \alpha A_3^4 \quad \text{and} \quad c_2^T = (1 - \alpha)A_3^4 + \alpha A_2^4.$$

There is about a 0.15% chance that one of these paths is part of a neighboring leaf, which seems to the authors akin to generating a four leaf clover. The chance of such an event is obviously dependent on the distribution and its parameters, and toying with alternatives leads to different qualities.

Paths within a leaf are generated with a uniform distribution, and in this example we use $\beta \sim U(2\eta, 1 - 2\eta)$, with $\eta = 0.0425$ as before. Each leaf has three or four paths internal to the leaf, and each of these is defined by a c vector of the form

$$c^T = (1 - \beta)A_i^4 + \beta A_j^4.$$

This stochastic process of path generation allows us to generate numerous patterns in a k -gon, and we use this technique in some of our projects.

Many of our patterns tile paths in adjoining polygons, but the resulting tilings are not polygonal per se. They are instead tilings of paths in polygons. This leaves patterns that only touch, or intersect, at terminal points of a path. Figure 7c is a version of the Pythagorean tiling and illustrates this phenomena. The Pythagorean tiling cascades two 4-gons, but the piece in Figure 7c is created by paths in the 4-gons, making the borders of the 4-gons intuitive even though they are not there.

Etchings and Laser Cutouts

The technique of generating random paths in a 4-gon extends directly to k -gons, and we have used this concept to promote math, art, and engineering to middle

school students during Rose-Hulman’s 2024 Sonia Math Day. We added an electrical engineering aspect to the project by designing a circuit that allowed participants to adjust parameters like k and the number of paths in a leaf, and they generated patterns until one struck their fancy. We etched these patterns onto colored acrylic medallions with a laser cutter to create backpack tags, resulting in mementos of a chic application of math and technology. Figure 6b is an example backpack tag of the paths in Figure 6a. We have also used patterns of central paths to etch leather to create coasters and key-chain fobs, and we have laser-cut wood trivets, see Figure 7. We continue to explore other possibilities, and in particular, we hope to tile glass etchings to create a work of stained glass. An acrylic prototype is in Figure 8.



(a) An etched leather coaster. (b) An etched key-chain fob. (c) A laser-cut wood trivet.

Figure 7: Art items created with a laser cutter/etcher.

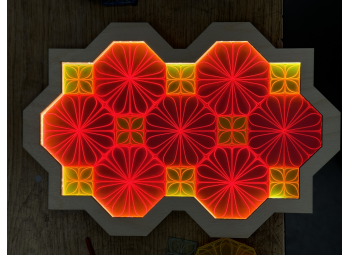
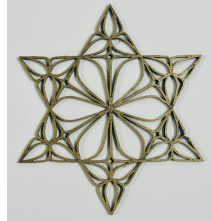


Figure 8: An acrylic prototype of a stained glass piece.

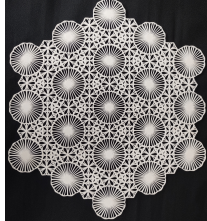
3D-Printing

3D-printers use several modalities to construct objects, and for the moment, we only consider the most common printing method of Fused Deposition Modeling (FDM). FDM printers are not capable of creating three-dimensional structures with paths in, for instance, a Platonic solid because they would require an impractical number of structural supports. However, modern FDM printers do provide a cost-effective way to create three-dimensional objects associated with two-dimensional patterns, which for us are tilings of central paths from k -gons. The printed items combine pattern, color, and shape, and we have used them as holiday decorations and decorative trinkets. We have also printed and assembled

random patterns to create a bouquet of daisy- and thistle-like objects, a project that we discuss below. Illustrative objects are in Figure 9.



(a) A holiday decoration.



(b) An intricate tiling.



(c) A bouquet.

Figure 9: FDM printed items.

Print Making with Cyanotype and SolarFast

Print making with patterns and/or tilings of two-dimensional central paths has become one of our favorite techniques. We use cyanotype and SolarFast, both of which are dyes that react with ultraviolet light to create color, to imprint patterns on paper and cloth. Cyanotyping is the original process used to make blueprints, and it only gives shades of blue. SolarFast is similar but comes in a variety of colors.

The technique begins with a design like the one in Figure 9b — we use a modern and accurate FDM printer. We note that the image processing software requires special settings to ensure fidelity to our mathematical calculations, for otherwise, the result is flawed with artifacts from aliasing. We then pre-stretch watercolor paper to reduce warping after the printing process. Colorless dye is then applied to the paper, and the 3D-printed pattern is placed over the dyed area. We subsequently expose the paper to sunlight for several minutes to create color in the unblocked regions. The print is then washed with a special soap and is left to dry. The drying process ends with improved flatness if the paper is held in place as it dries. The results are, at least to the authors, visually stunning, see the previously published pieces in Figure 10 as examples¹. A piece similar to Figure 10a, but with a solid, dark-blue background, is also now part of Rose-Hulman’s permanent art collection.

We used the SolarFast print making process to promote mathematics to middle school students during Rose-Hulman’s 2025 Sonia Math Day. Students selected from patterns after learning about central paths, and they then applied SolarFast Dye to a 4 inch by 6 inch piece of watercolor paper. We then exposed and washed their prints, and everyone left with a unique piece of art to remember the day. The collection of pieces is in Figure 11a. We have also used SolarFast

¹Both images published in [8] and reused here with the authors’ permission.



(a) Uniform Paths in a 3-4-3-12 Tiling with Blue Green Squiggle Background [8]. (b) Uniform Paths in a Truncated Trihexagonal Tiling with Nebular Background [8].

Figure 10: Prints made with SolarFast.

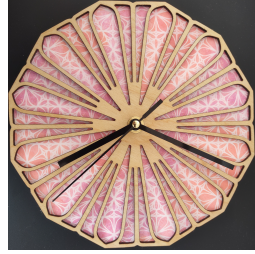
dye to imprint t-shirts and other cloth items, and Figure 11b shows the front and back of a shirt.



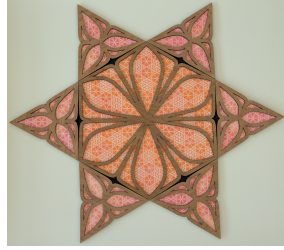
(a) Art projects from Rose-Hulman's 2025 Sonia Math Day. (b) T-shirt printing.

Figure 11: SolarFast projects and a cloth example.

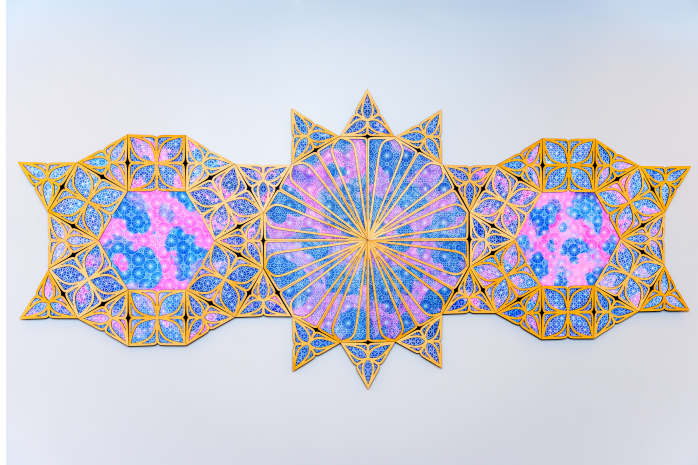
Combining prints and wood cuttings elevates the visual effect. These pieces have a SolarFast print behind a laser-cut wood pattern, rendering a collection of “windows” through which the colored patterns are visible. Figure 12 contains two examples. The wood portion of the clock in Figure 12a has paths in a 12-gon, with each leaf having four paths. The red-orange SolarFast background of the clock is a tiling of paths in hexagons and triangles. The large wall piece in Figure 12c is over 10 feet long and 4 feet tall. The wood is maple veneered, 1/4-inch plywood finished with linseed oil, and the piece has 26 triangular patterns, 12 square patterns, and one 12-gon pattern. The colorful SolarFast backdrop is created from tilings with paths in 3-, 4-, 6-, 8-, and 12-gons. This piece of art is part of Rose-Hulman’s permanent collection, and a discussion of the artistic techniques and efforts is in the attached supplement.



(a) A wall clock.



(b) A medium wall piece.



(c) A large wall piece.

Figure 12: Pieces that combine SolarFast print making with wood cuttings.

4.2 Three-Dimensional Art

Three-dimensional objects are visually possible as digital images, but many are difficult to physically produce without special consideration and equipment. The most immediate issue is that FDM printers limit structure because they do not naturally accommodate overhanging features without additional, awkward, and unwanted vertical supports. This restriction limits creating three-dimensional renderings of paths in a polytope, such as a Platonic solid, with standard FDM printers. We have had success with selective laser sintering (SLS) printing, but we postpone that discussion and focus momentarily on three-dimensional items possible with FDM printers.

A 3D printer requires a standard triangle language (stl) file that approximates the surface of the object being printed, but curves in three-dimensional space have no surface. Moreover, there are no standard python packages that generate printable stl files from parametrized curves, and as such, we created a

custom package to generate printable files. The mathematical routine is simple in concept, as it essentially turns each path into a spaghetti-like object whose surface is then approximated by a triangulation, which is then 3D printable. We accomplish this task by identifying a collection of points on the path, computing a unit normal vector to the path at that point, and then placing points on a circle that is centered at the point on the path and that passes through the terminal end of a scaled version of the normal vector. This process “extrudes” a circle along the central path, with the result being a collection of points on the surface of a thickened version of the path, from which we create a triangulation for printing.

Daisies and Thistles

Daisies have relatively flat petal arrangements, which makes them easy to imitate with two-dimensional patterns in k -gons. We adjoin a three-dimensional central path as stem to complete the facsimile. The simplicity of this design allows us to print daisies with an FDM printer so long as the central path forming the stem has limited overhang/bend. Another option is a thistle. We mimic the spiky nature by setting $G(x) = x_1^2 + x_2^2 - 1$ to get a unit disc. Solving (3) shows that

$$\overline{\mathbf{P}(G(x), c)} = \left\{ x(\mu) = \frac{\sqrt{\mu^2 + \|c\|^2} - \mu}{\|c\|^2} c : \mu > 0 \right\} \cup \left\{ 0, \frac{c}{\|c\|} \right\},$$

and hence, central paths in a disc are (unsurprisingly) straight lines. We comment that this fact is true for any two-norm unit sphere in higher dimensions. Figure 13 displays FDM printed items.



(a) FDM daisy. (b) FDM thistle.

Figure 13: FDM prints of a daisy and a thistle.

SLS Printing

Selective laser sintering (SLS) printing gives a significant advantage over other three-dimensional printing modalities because it forms a mold of the item as it is being printed, and hence, there is no need for additional supports. SLS printers build an item in layers similar to other printing paradigms, but SLS printing deposits a uniformly thin layer of polyamide material that is then fused with a laser to create a horizontal slice of the item(s) being printed. The unused

polyamide material remains in place until the print is complete, creating a mold that supports the object. So SLS printers can print space-curves from stl files that approximate the curves. An SLS printer was unfortunately outside our funding ability, but we were able to pay a third party to create a single print. We selected random paths in a cube as our first test case because these images started our project. Figure 14 shows the original three-dimensional image and the SLS print. We comment that the SLS print is not cubic although the stl file indicated that it should have been. We suspect that either the printer or the vendor reduced the vertical direction due to machine limitations or production restrictions.



(a) An stl image of a cubic flower. (b) An SLS printed cubic flower.

Figure 14: An example of SLS printing.

5 Conclusion and Future Goals

We promote that the central path is a thing of beauty and is worthy of artistic exploration. Its revolutionary impact on the field of optimization is, in itself, an esoteric and rigorous work of art, but we have now shown that the central path is also a unique ‘brush stroke’ with which we can create items of physical beauty. The mathematics of the central path controls these two- and three-dimensional constructs, and we manifest brush strokes by changing mathematical models. So in this project, artistic modeling is mathematical modeling, and the bridge between the two paradigms is a significant amount of computing.

Our primary goal for the future is to advance our ability with SLS printing, and in particular, we hope to create a large optimization garden full of flower-like objects. Much of the mathematical and computational effort is in place, and we have, for instance, developed code to generate paths in the five Platonic solids. The authors have found this effort to be a unique mathematical enterprise because, while optimizers and geometers have long known how to express polytopes in terms of either facet inequalities or as convex combinations of vertices, going from one to the other has been a chore even though the mathematical relationships are well understood. Descriptions of the Platonic solids are commonly expressed in terms of standardized coordinates, i.e. in terms of vertices, but our mathematical models require facet inequalities. We initially

formulated a linear combinatorial problem whose solution was a normal to a facet, and while this problem worked well on the tetrahedron and the cube, it proved insufficient or impossible to solve on the octahedron, the dodecahedron, and the icosahedron. So we moved to a search over subsets of the vertices to identify which subsets defined facets, from which we could then calculate a facet normal. This proved efficient on all five solids.



(a) An stl image of a tulip.

(b) A rosebud.

Figure 15: Digital renderings for potential SLS printing.

The SLS print in Figure 14b illustrates possibility, but this flower is surely, and wonderfully to the authors, a bit Burtonesque. The tulip and rosebud images in Figure 15 are more realistic, but we are not yet able to print these items. Theorem 6 establishes that we can create a surface of paths for the petal of a tulip, and we use our previous thickening technique on a discrete collection of paths to emulate a petal. The result is an stl file like the one in Figure 15a. This technique unfortunately renders a file with an excessively large triangulation due to the numerous intersections among the paths, and our printing software is unable to slice the object for printing. We hope to overcome this issue soon by extending our triangulation software to avoid overlaps and intersections. The rosebud in 15b is created by paths in a tetrahedron, and while our thickening technique should work similar to the item in 14b, we have not yet generated stl files because we do not have access to an SLS printer. There is much more to explore, and in particular, we plan to learn which shapes lend themselves to SLS printing, what materials and finishes work well and give lasting results, and which computational adjustments ensure/advance the mathematical fidelity of the printed items.

Acknowledgments: The authors thank Ms. Souilly Abas, Associate Professor of Art, and Ms. Christy Brinkman-Robertson, Art Curator, both at the Rose-Hulman Institute of Technology. Their support, encouragement, and guidance have been invaluable.

References

- [1] R. Caron, H. Greenberg, and A. Holder. Analytic centers and repelling inequalities. *European Journal of Operational Research*, 143(2):268–290, 2002.
- [2] A. Deza, E. Nematollahi, R. Peyghami, and T. Terlaky. The central path visits all the vertices of the Klee-Minty cube. *Optimisation Methods and Software*, 21(5):851–865, 2006.
- [3] I. Dikin. Iterative solution of problems of linear and quadratic programming. *Soviet Mathematics. Doklady*, 8:674–675, 1967.
- [4] A. Fiacco and G. McCormick. *Nonlinear Programming: Sequential Unconstrained Minimization Techniques*. Wiley, 1968. reprinted, Classics Applied Mathematics, SIAM, Philadelphia, 1990.
- [5] A. Forsgren, P. Gill, and M. Wright. Interior methods for nonlinear optimization. *SIAM Review*, 44(4):525–597, 2002.
- [6] R. Frisch. The logarithmic potential method for solving linear programming problems. *Memorandum from Institute of Economics*, 1955.
- [7] P. Gill, W. Murray, M. Saunders, J. Tomlin, and M. Wright. On projected Newton barrier methods for linear programming and an equivalence to Karmarkar’s projective method. *Mathematical Programming*, 36(2):183–209, 1986.
- [8] C. Tasik & InteriArt Research Group. *Ink: Rose-Hulman’s Literary and Visual Arts Magazine. Ink*, vol. 23, 2025. www.rose-ink.wixsite.com/home.
- [9] M. Halická. Analytical properties of the central path at boundary point in linear programming. *Mathematical Programming*, 84(2), 1999.
- [10] A. Holder. Simultaneous data perturbations and analytic center convergence. *SIAM Journal on Optimization*, 14(3):841–868, 2004.
- [11] A. Holder and R. Caron. Uniform bounds on the limiting and marginal derivatives of the analytic center solution over a set of normalized weights. *Operations Research Letters*, 26(2):49–54, 2000.
- [12] P. Huard. Resolution des programmes mathematiques par la methode des centres. Technical report, Note E.D.F. HR 5690, 1964.
- [13] P. Huard. Resolution of mathematical programming with nonlinear constraints by the method of centers. In *Nonlinear Programming*, pages 207–219. North Holland, 1967.
- [14] F. Jarre, G. Sonnevend, and J. Stoer. An implementation of the method of analytic centers. In A. Bensoussan and J. Lions, editors, *Analysis and Optimization of Systems*, pages 295–308, Berlin, Heidelberg, 1988. Springer Berlin Heidelberg.

- [15] N. Karmarkar. A new polynomial-time algorithm for linear programming. *Combinatorica*, 4:373–395, 1984.
- [16] N. Karmarkar. A new polynomial-time algorithm for linear programming. In *Proceedings of the sixteenth annual ACM symposium on Theory of computing*, pages 302–311, 1984.
- [17] L. Khachiyan. A polynomial algorithm in linear programming. *Soviet Mathematics. Doklady*, 20:191–194, 1979.
- [18] V. Klee and G. Minty. How good is the simplex algorithm? In O. Shisha, editor, *Inequalities III*, page 159–175. Academic Press, 1972.
- [19] J. De Loera, B. Sturmfels, and C. Vinzant. The central curve in linear programming. *Foundations of Computational Mathematics*, 12(4):509–540, 2012.
- [20] E. Nematollahi and T. Terlaky. A simpler and tighter redundant Klee-Minty construction. *Optimization Letters*, 2:403–414, 2008.
- [21] C. Roos, T. Terlaky, and J-Ph Vial. *Interior point methods for linear optimization*. Springer Science & Business Media, 2005.
- [22] J. Sauppe, editor. *Mathematical Programming Glossary*. INFORMS Computing Society, <http://glossary.informs.org>, 2006–24. Originally authored by Harvey J. Greenberg, 1999–2006.
- [23] G. Sonnevend. An “analytical centre” for polyhedrons and new classes of global algorithms for linear (smooth, convex) programming. In *System Modelling and Optimization. Lecture Notes in Control and Information Sciences*, volume 84, pages 866–875, Berlin, Heidelberg, 1986. Springer, Springer Berlin Heidelberg.
- [24] G. Sonnevend. New algorithms in convex programming based on a notion of “centre” (for systems of analytic inequalities) and on rational extrapolation. In *Trends in Mathematical Optimization: 4th French-German Conference on Optimization*, pages 311–326. Springer, 1988.
- [25] Tamás Terlaky. Twenty-five years of interior point methods. In *Decision Technologies and Applications*, pages 1–33. INFORMS, 2009.
- [26] S. Vavasis and Y. Ye. A primal-dual interior point method whose running time depends only on the constraint matrix. *Mathematical Programming*, 74(1):79–120, 1996.
- [27] M. Wright. The interior-point revolution in constrained optimization. In *High Performance Algorithms and Software in Nonlinear Optimization*, pages 359–381. Springer, 1998.

- [28] M. Wright. The interior-point revolution in optimization: history, recent developments, and lasting consequences. *Bulletin of the American Mathematical Society*, 42(1):39–56, 2005.
- [29] Margaret H Wright. Some properties of the Hessian of the logarithmic barrier function. *mathematical Programming*, 67(1):265–295, 1994.
- [30] Stephen J Wright. Modified Cholesky factorizations in interior-point algorithms for linear programming. *SIAM Journal on Optimization*, 9(4):1159–1191, 1999.

Supplement: Artistic Techniques and Lessons

We present in this supplement the artistic techniques used to create the large piece of art in Figure 12c. The scale of this project challenged our intent to use what we had learned from smaller works to create an expansive piece for a spacious and well-traveled hallway. Techniques that had been successful for moderate pieces just didn't scale easily, and we spent months tinkering with software, 3D printers, laser cutters, and dyeing processes before gaining the finesse to create a professional product. We catalog our methods here to aid others interested in similar projects.

This work combined three components, those being wood cutouts of central paths for the front facing ‘frames,’ 3D printed tilings to emboss patterns on the underlying paper, and the dyeing process to create the dynamic of color. We address each of these processes below.

5.1 Wood Cutouts

We started with a collection of paths in a k -gon for each wood frame, but these paths are mathematically one-dimensional and have no area, which means that they cannot be used to create wood frames without imposing a width, i.e. we needed to ‘thicken’ the paths. We saved each image as a scalable vector graphic (svg) file and used the open-source svg editor Inkscape to thicken the paths. The automated process in Inkscape unfortunately left the corners empty as seen in Figure 16a. The light-blue curves are our computed central paths, and the larger dark-blue areas are Inkscape’s thickened versions. The intersection of the thicker paths left voids at the corners that we had to manually correct in each image, see Figure 16b. We then used a laser cutter to cut wood frames that tiled without awkward gaps.

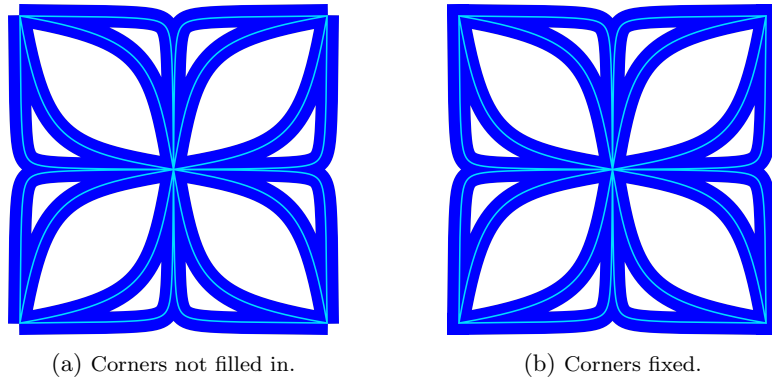


Figure 16: Light blue original paths and dark blue thickened paths.

5.2 SolarFast Dyeing

John Herschel invented solar/sun prints, called cyanotypes, in the 1840s, which he produced by saturating a piece of paper or cloth with a mixture of ferric ammonium citrate and potassium ferricyanide and then exposing the saturated item to UV light. The chemicals reacted under this exposure and dyed the item blue, with blueprints being an early example of the technique. A downside of cyanotyping is that we only have the single color of blue, but we fortunately have a similar contemporary process that uses SolarFast that permits a variety of colors. We have experimented with both cyanotypes and SolarFast, and we generally prefer SolarFast.

3D Patterns

The svg files of 2D patterns, like the ones that we used for laser cuttings, are not directly 3D printable because a thickened path in two-dimensions has no volume, and 3D prints require surfaces of volumes. We have already noted our custom software that extrudes circles along a path to create a printable stl file in Section 4.2. This code also works for paths in two-dimensions by setting the vertical z -coordinate to zero, but it does so in a way that leaves the three-dimensional tessellations of the thickened paths shy of being horizontally flat. We have instead used standard software in, for instance, our printer's suite of utilities that accepts 2D svg images and thickens them vertically for printing. This has proven trustworthy and has given us control of the vertical height of the print, which is an important design element for the dyeing process.

The 3D printed patterns of the dyeing process are negatives because they shield ultraviolet exposure and leave an undyed pattern. The general process is to apply dye to watercolor paper, which is colorless at that point, place a 3D printed pattern on the paper, cover the pattern with thick glass to hold everything in place, expose the paper to sunlight to activate the chemicals and create color, and then wash and dry the paper. This straightforward process works well for smaller items, but it requires special attention as it scales for larger pieces. The most daunting concern is that large pieces of watercolor paper tend to warp and shrink as they are exposed, leaving the negative less than effective. The flawed result has weak-looking paths that lack contrast and that tarnish the visual acuity of the underlying mathematics. We discovered solutions to several design decisions to remove, or at least limit, this concern.

The type of watercolor paper is important, and for larger pieces we found that 140 pound cold-pressed paper with a composition of 25% cotton works well. Heavier weights like 300 pound paper can work nicely because they reduce buckling; however, their heavier weight challenges gluing them to the wooden frames even with reduced buckling. We experienced more buckling with lighter weight paper but were able to better press the print flat as we glued it to the frame, creating a polished and taught appearance. Using a cold-pressed paper gave us a slightly textured surface that worked well with SolarFast.

The negatives of our largest prints exceeded the dimensions of our FDM

printer, and as such, we printed the negatives in pieces that were then welded together with a soldering iron to create one large pattern, see Figure 17. The dimensions of the paths and the type of filament are both important for fitment and dyeing. We have used both PLA and PETG filaments, but we prefer PETG because it has thermal properties that allow the reuse of the pattern. PLA patterns actually work a bit better for large prints because they conform better to the surface of the paper, but they warm and deform during the exposure period, leaving them questionable for subsequent prints. So PLA patterns work well but create waste and lengthen the creative timeline due to the need to print and assemble a new pattern for each print. The dimensions of the 3D printed paths are important because the width defines what the eye will see of a path, and the height alters how sunlight will interact with the dye. We have found that PETG with a path width varying from 1 to 1.2mm and a vertical height of 1.5mm results in a negative that has accurate fitment and balanced flexibility, resulting in prints with good visual acuity and contrast.

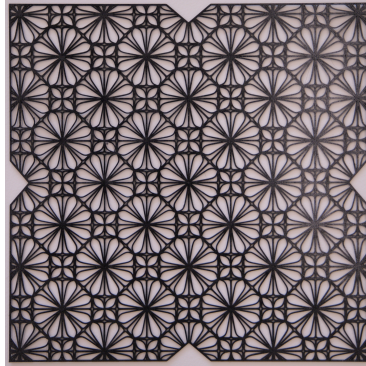


Figure 17: 3D Printed Negative.

Solar Printing

The general printing process described above has several smaller but important steps if the goal is to create high-quality large prints. The most important hindrance to overcome is the fact that the paper adjusts as it warms during the exposure period. We warn that we tried several ways of immobilizing the paper to limit the deleterious effect of exposing the paths that were supposed to be shielded by the negative. None of holding the paper taught with tape, adding additional glass for extra weight, or padding the backside of the paper to help impress the negative worked individually. The tension created by the warming paper is impressive, and attempts to physically affix it proved ineffective. What instead worked was to delay the paper's deformation by keeping it wet during the dyeing process. We accomplished this task by wetting the paper prior to dyeing it, which left the paper sufficiently wet during the exposure that it did

not appreciably deform. This technique, along with some physical binding, gave excellent results. Our standard procedure for large prints is below.

1. Soak the paper in water for five to ten minutes.
2. Combine dye and water in small bowls or containers in a roughly 2:1 ratio.
3. Brush dye onto paper with a one-inch foam brush, with each color getting its own brush.
4. Lightly mist the paper with water using a spray bottle.
5. Use a two-inch round sponge to blot the paper, remove brush strokes, and spread the color (in a quasi-random way).
6. Place the paper on a flat padded surface.
7. Place the 3D printed negative on top of the paper.
8. Use your hands or a rubber brayer to slightly press the negative onto the wet paper, which somewhat adheres the negative to the paper.
9. Place a piece of glass on top of the negative and press down firmly. Multiple pieces of glass for extra weight can help.
10. Take the piece outside and expose it in a shady spot for around twenty minutes - longer if the UV index is low. The print is done once you are happy with the color.
11. Bring the print back inside and wash it following the SolarFast instructions. Make sure the print does not become translucent while washing it. Stop washing immediately if so.
12. Place the washed print on a stretching board.
13. Wipe the surface of the paper to remove any remaining dye with a dry paper towel.
14. Tape the edges of the paper to the stretching board and wait for the print to dry.

We comment that pre-soaking the paper affects the color of the dye, and most notably, it results in the color being truer to the advertised hue. We suspect that this effect is due to the extra dilution of the dye, but it could also be due in part because the dye absorbs deeper into the paper. In any event, the concentration of the dye is an important consideration of an artist as they use this technique.